Facile synthesis of cobalt-doped $Ni_3(NO_3)_2(OH)_4$ porous nanosheets for high-performance supercapacitors

Lingli Xie[1], Mingjie Shi[2,3], Hideo Kimura[2], Mangwei Cui[4,5], Kai Wang[1], Baoyin Cui[1], Wei Du[2], and Litao Kang[2,*]

[1] *Department of Materials Engineering, Taiyuan Institute of Technology, Taiyuan 030008, China*

[2] *College of Environment and Materials Engineering, Yantai University, Yantai 264005, China*

[3] *Weichai Balllard Hydrogen Technology Co., LTD, Weifang, China*

[4] *College of Materials Science and Engineering, Taiyuan University of Technology (TYUT) Taiyuan, Shanxi 030024, China*

[5] *School of Materials Science and Engineering, Harbin Institute of Technology (Shenzhen), Shenzhen 518055, China*

ABSTRACT

As an emerging electrode material of supercapacitors, $Ni_3(NO_3)_2(OH)_4$ holds remarkable merits including environmental friendliness, large layer spacing ($c = 6.9$ Å), and high specific capacitance. Nevertheless, its rate capability and cycling stability have yet to be improved. Herein, a simple Co-doping strategy is introduced into the solution combustion preparation process to solve these problems. The optimized Co-doping dosage is determined to be 15 at.%, based on electrochemical performance test. The doped cobalt improves not only the rate capability by increasing electronic and ionic conductivity, but also the cycling stability by enhancing structural stabilization. Thanks to the benefits of Co-doping, the optimized sample simultaneously achieves high specific capacitance (1579 F/g at 1 A/g), excellent rate capability (78.3% capacity remains when current density increases from 1 to 20 A/g), and decent cycling stability (85.7% capacitance retention after 5000 cycles). At even an ultrahigh mass loading of 15.05 mg/cm^2, the specific capacitance remains still significant (1062 F/g at 1 A/g). When coupled with a commercial activated carbon electrode, the resulting asymmetric capacitor delivers a remarkable energy density of 26 Wh/Kg at a power density of 2766 W/Kg.

Lingli Xie and Mingjie Shi contributed equally to this paper and are co-first authors.

Address correspondence to E-mail: kanglitao@ytu.edu.cn

1 Introduction

Supercapacitors are one kind of vital equipment to clean energy storage, thanks to their high-power density, fast charging ability, and long cycle life [1–3]. As an important component of supercapacitors, electrode materials have significant impact on the performance of the devices [4]. In recent decades, the development of high-performance electrode materials is constantly attracted intense attentions. Transition metal oxides/hydroxides, as one kind of promising electrode materials, use the 2D (two-dimensional) or quasi-2D surficial redox reactions to storage charges, which thereby generate faraday pseudocapacitance far larger than the electric double layer capacitance [5].

Among various transition metal oxide/hydroxide electrodes, nickel-based transition metal hydroxides are especially attractive, due to their highly accessible valence variation, high theoretical specific capacity and affordable cost [6, 7]. In previous work, we developed a facile solution combustion method to synthesize feather-like $Ni_3(NO_3)_2(OH)_4$ nanosheets with high capacitance [8]. This synthesis process is advantageous in synthesis efficiency, scalability to mass production, and flexibility of composition control [9]. Nevertheless, the rate capability and especially cycling stability are not fully satisfied [10–13]. This situation will be even worse at high mass loading of active material on the electrodes, because the thick electrode material layer amplifies the negative influence of poor electrical conductivity and structural degradation. In this regard, foreign element doping is regarded as a promising strategy since it can not only stabilize the host materials' structures but also boost their electrical conductivity [12, 14–17]. Recently, numerous studies have shown that Co-doping is highly effective to improve the electrochemical performance of a variety of electrode materials [15, 18–22]. The performance improvements are always attributed to the doping-introduced bandgap narrowing and electrical conductivity increase, which greatly improve reaction kinetics [16, 17]. Moreover, Co-doping can stabilize the octahedral framework of $Ni_3(NO_3)_2(OH)_4$ crystallographic structure, by means of mitigating the Jahn–Teller effect, very favorable to improving the cycling stability of this material [6, 23–25].

Herein, $Ni_3(NO_3)_2(OH)_4$ electrodes with different Co-doping dosages are synthesized by facilely modifying the solution combustion method. The successful doping of cobalt elements is confirmed by XRD, EDS and XPS. The effects of Co-doping dosage on the electrochemical properties of $Ni_3(NO_3)_2(OH)_4$ are systematically investigated with systematic electrochemical tests. The 15 at.% Co-doped $Ni_3(NO_3)_2(OH)_4$ exhibits the best rate capability (78.3% capacity remains when current density increases from 1 to 20 A/g) and cycling stability (85.7% capacitance retention after 5000 cycles at 10 A/g), 32.8% and 13.0% higher than its undoped counterpart, respectively. Even at a very high mass loading of 15.05 mg/cm², the specific capacitance remains still significant (1062 F/g at 1 A/g). Finally, a high-performance asymmetric supercapacitor is assembled with the Co-doped cathode and activated carbon (AC) anode, achieving an high energy density of 26 Wh/Kg at a power density of 2766 W/Kg.

2 Experimental methods

2.1 Synthesis of Co-doped $Ni_3(NO_3)_2(OH)_4$

The $Ni(NO_3)_2 \cdot 6H_2O$ was prepared by a facile solution combustion method, as described in our previous work [8]. Briefly, 3 g of nickel nitrate hexahydrate ($Ni(NO_3)_2 \cdot 6H_2O$) and 0.826 g of urea ($CO(NH_2)_2$) were dissolved in 20 ml deionized water under magnetic stirring. Then, different amounts of cobalt nitrate hexahydrate ($Co(NO_3)_2 \cdot 6H_2O$, 0.15 g, 0.3 g, 0.45 g and 0.6 g, corresponding to Co/Ni molar ratios of 5%, 10%, 15%, 20%, respectively) were separately added into the nickel nitrate/urea solution. After thorough mixing and dissolving, the mixed precursor solution was directly heated at 250 °C for 30 min with a heating rate of 7.5 °C/min. Finally, the obtained black green powder was washed with deionized water and ethanol for several times, before drying at 70 °C for 12 h. To simplify discussion, all samples were named after the Co/(Ni+Co) molar ratios in percentage. For example, sample 15 means the Co-doping dosage is 15 at.%.

2.2 Structural characterizations

The X-ray diffraction pattern of the Co-doped $Ni_3(NO_3)_2(OH)_4$ was collected on a DX-2700 X-ray diffractometer. The morphology of samples was observed on a Mira3 microscope (FESEM) equipped

with an Oxford X-ray energy-dispersive spectrometer (EDS). X-ray photoelectron spectrum (XPS) was collected by a K-Alpha system (Thermo-Fisher); the binding energy of the XPS data was calibrated using the C1s peak (284.6 eV) as an internal standard. N_2-sorption isotherm was acquired at 77.3 K by using an Autosorb Gas Sorption System. The isotherms were analyzed by the Brunauer–Emmett–Teller (BET) and the pore diameter distributions were obtained from the adsorption branch via the Barrett–Joyner–Halenda (BJH) model.

2.3 Electrochemical characterizations

2.3.1 Electrode test

To prepare working electrodes, coating slurries were firstly fabricated by mixing active materials (i.e., the $Ni_3(NO_3)_2(OH)_4$ samples, or the employed activated carbon), acetylene black and polyvinylidene difluoride (PVDF, in N-methyl pyrrolidone solvent with a solid content of 20 g/L) at a weight ratio of 8:1:1. The slurry was pasted on Ni foams (1×2 cm^2) current collectors and dried in air at 70 °C for 12 h. The coated Ni foams were pressed at 10 MPa for 10 s to prevent the active material from peeling.

For electrochemical measurements, cyclic voltammetry (CV, 0–0.7 V) and galvanostatic charge–discharge (GCD, 0.1–0.55 V) curves of working electrodes were collected by using a three-electrode test method on an electrochemical workstation (CHI-660D, Chenhua, Shanghai). A Hg/HgO electrode, a 2×2 cm^2 platinum foil, and 1 mol/L LiOH aqueous were employed as reference electrode, counter electrode, and electrolyte, respectively. The specific capacitance (C, F/g) was calculated by Eq. (1) and the measured GCD [26]:

$$C = \frac{I\Delta t}{m\Delta V},$$
(1)

where C (F/g) is the specific capacitance, I (A) is the discharge current, Δt (s) is the discharge time, ΔV (V) is the width of potential window and m (g) is the mass of the active material in the electrode.

2.3.2 Asymmetric supercapacitor test

A CR-2025 button cell was assembled with a Co-doped $Ni_3(NO_3)_2(OH)_4$ positive electrode ($\varphi = 16$ mm), a commercial activated carbon (AC,

Fuzhou Yi Yuan Carbon limited Co. Ltd.) negative electrode, a polypropylene separator (Nagano Industries Co., LTD, $\varphi = 19$ mm), and the 1 M LiOH electrolyte. The electrochemical performance of this cell was tested on a CT2001A battery testing instrument. To balance the charge storage capacity of the positive and negative electrode, the mass loading ratio of these electrodes are fixed at a certain ratio determined by the following Eq. (2) [27, 28]:

$$\frac{m_{cathode}}{m_{anode}} = \frac{C_{anode} \times \Delta V_{anode}}{C_{cathode} \times \Delta V_{cathode}},$$
(2)

where C (F/g) is the specific capacity of the electrode material, ΔV (V) is the operational voltage window of the corresponding electrode, m (g) is the loading mass of active materials on the electrodes.

The energy density (E, Wh/Kg) and power density (P, W/Kg) of the asymmetric supercapacitor were calculated according to the following Eqs. (3–4)[29], based on the total mass of active materials on both positive and negative electrodes.

$$E = \frac{1}{3.6} \int_{t1}^{t2} \frac{IV}{m} dt,$$
(3)

$$P = \frac{E}{\Delta t},$$
(4)

where I (A) is the discharge current, V (V) is the voltage window of the cell, m (g) is the total loading mass of active material on the two electrodes, t_2-t_1 (s) represents the discharge time, Δt (h) is the discharge time corresponding to energy density E.
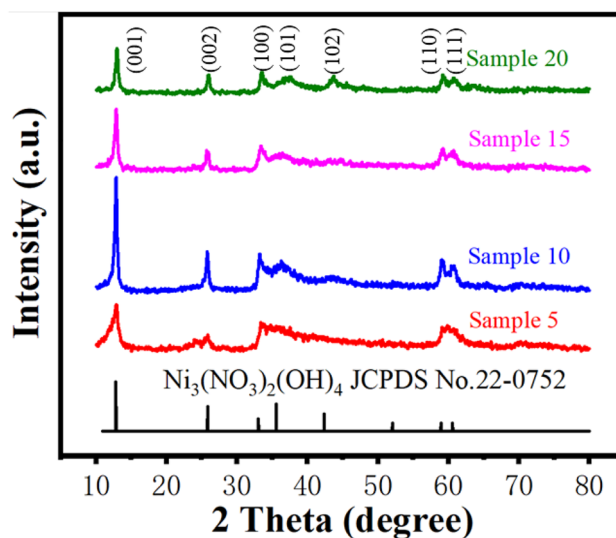

Fig. 1 XRD patterns of samples with different Co-doping dosages

3 Results and discussion

3.1 Structure and phase characterization

Figure 1 displays the XRD spectra of the Co-doped $Ni_3(NO_3)_2(OH)_4$ samples. After Co-doping, the samples still adopt a hexagonal $Ni_3(NO_3)_2(OH)_4$ phase (JCPDS No. 22–0752, $a = b = 3.131$ Å and $c = 6.898$ Å) [11, 30]. In addition, no impurity signals (e.g., cobalt or nickel oxide) were detected in these XRD patterns, indicating the successful doping of cobalt into the $Ni_3(NO_3)_2(OH)_4$ lattice [31–33]. As a result, the diffraction peaks on the crystal planes (101) and (102) slightly red-shifts as the doping dosage increase.

Figures 2a–d depict the elemental mapping of Sample 5–20 determined by the EDS technique. In all samples, the Ni, Co, O, and N elements distribute homogeneously in the entire measured area. In line with the XRD results, the data also confirm the absence of phase separation or element aggregation. Figure 2e–h further exhibits the SEM images of these samples, which show an irregular granular morphology of solution combustion products. There are numerous interstices between the sub-micro particles, providing plenty of interfaces for electrode/electrolyte contacting and reaction, besides shortening the diffusion distance of the charge-carrying ions. This microstructure should be useful for the achievement of high-rate capability and excellent specific capacitance.

XPS tests were performed on two typical samples, Sample 5 and 15 (Fig. 3a–d). In the XPS spectra, signals from Ni, O, N, and Co elements were clearly detected, in agreement with the XRD and EDS results. Figure 3a indicates the high-resolution XPS spectra of Ni2p orbital. Both samples consist of two spin orbitals, $Ni2p_{3/2}$ and $Ni2p_{1/2}$ located at 855.6 eV and 873.2 eV, respectively. The separation energy of these two orbitals is 17.7 eV, suggesting a chemical state of Ni^{2+} [9]. The Co2p high-resolution spectrum shows the $Co2p_{3/2}$ and $Co2p_{1/2}$ peaks at 781.4 eV and 796.7 eV respectively (Fig. 3b), matching well with the binding energy of Co^{2+} [34, 35]. The O1s spectra can be divided into the O–H bond (531.6 eV) [36] and O–N bond (532.8 eV) in both samples (Fig. 3c) [37]. However, the binding energies of Sample 5 and 15 has a little deviation, probably because the different Co^{2+} doping dosages have some effect on the chemical state of those atoms. The N1s peaks of the two samples in Fig. 3d stem from the N–O bond of NO_3^- (406.7 eV) [37].

The specific surface area and pore structure of pseudocapacitive materials have beneficial effects on their electrochemical properties. Figure 4 illustrates N_2-sorption isotherms and pore size distribution curves (insets) of these samples. All sorption isotherms belong to type IV featured a clear hysteresis loop between a relative pressure (P/P_0) of 0.4–1.0 [38], suggesting a mesoporous structure. As expected, the pores in these samples mainly distribute in a range < 20 nm, a proper size to ensure both fast electrolyte transport and high specific area.

Table 1 shows the BET-determined pore structure parameters of all samples. In general, the specific surface area and pore volume of the doped samples decrease with the increase of Co-doping dosage. On one hand, the decrease of pore volume increases the apparent densities of electrode materials, conducive to achieving higher volumetric energy densities. On the other hand, the decreased specific surface area and pore volume may limit the accessibility of electrolytes, resulting in low capacitances.

3.2 Electrochemical characterization

In order to investigate the influence of Co-doping on electrochemical performances, CV and GCD tests of these samples were performed and collected through a conventional three-electrode system. As shown in Fig. 5a, all samples demonstrate a pair of distinct redox peaks, corresponding to the charge/discharge plateaus of the GCD curves (Fig. 5b). It is the typical behavior of pseudocapacitive compounds resulting from a charge transfer reaction or electrochemical absorption/desorption process at the electrode/electrolyte interface [15]. According to literature, the doped Co atom may also participate in the redox reaction, and the cobalt–nickel bimetallic synergy increases the active sites for chemical reactions and improves the specific capacitance [39]. According to Eq. 1, the specific capacities of Sample 5, 10, 15 and 20 are determined to be1321.1, 1326.7, 1447.8 and 1035.6 F/g, respectively, at a current density of 5 A/g.

Figure 5c shows the rate performance of all samples. When the current density was increased from 1 to 20 A/g, the specific capacitance retention of Sample 0, 5, 10, 15 and 20 were 45.6%, 58.3%, 78.1%, 78.3%, and 68.3%, respectively. Therefore, both capacitance and rate capability test confirm the beneficial effect of Co-doping on the electrochemical performances of $Ni_3(NO_3)_2(OH)_4$ electrodes [8].
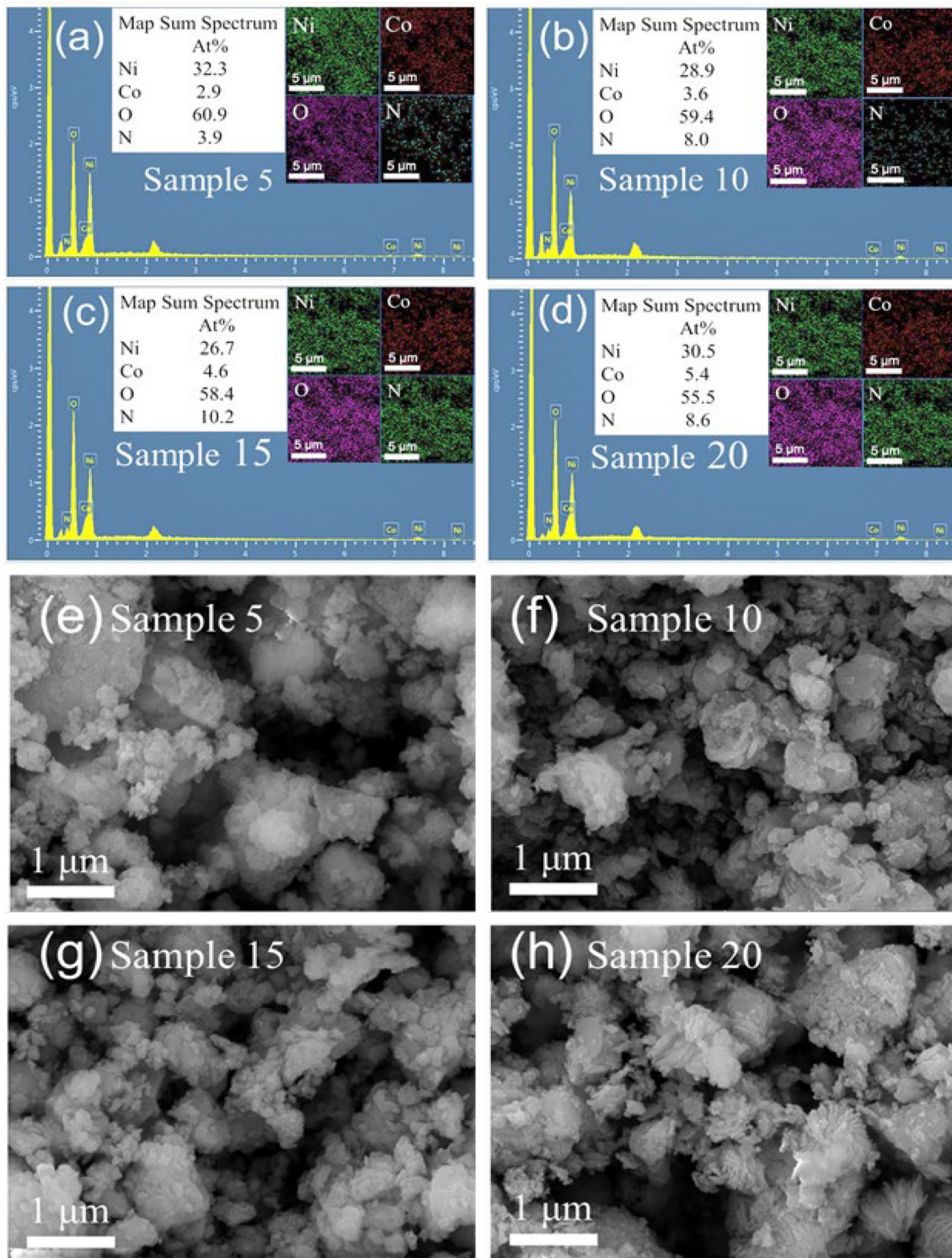
Fig. 2 **a–d** Elemental mapping and **e–h** SEM images of Sample 5, Sample 10, Sample 15 and Sample 20, respectively

To further explore the reasons of performance improvement introduced by Co-doping, EIS tests were conducted on the five samples, as shown in Fig. 5d. The curves of all samples include two parts, the semicircular arc in the high-frequency region and the diagonal line of the low-frequency region. Among them, the diameter size of the semicircular arc in the high-frequency region represents the charge transfer

Fig. 3 High-resolution spectra of Ni2p **a**, Co2p **b**, O1s **c** and N1s **d** of Sample 5 and Sample 15
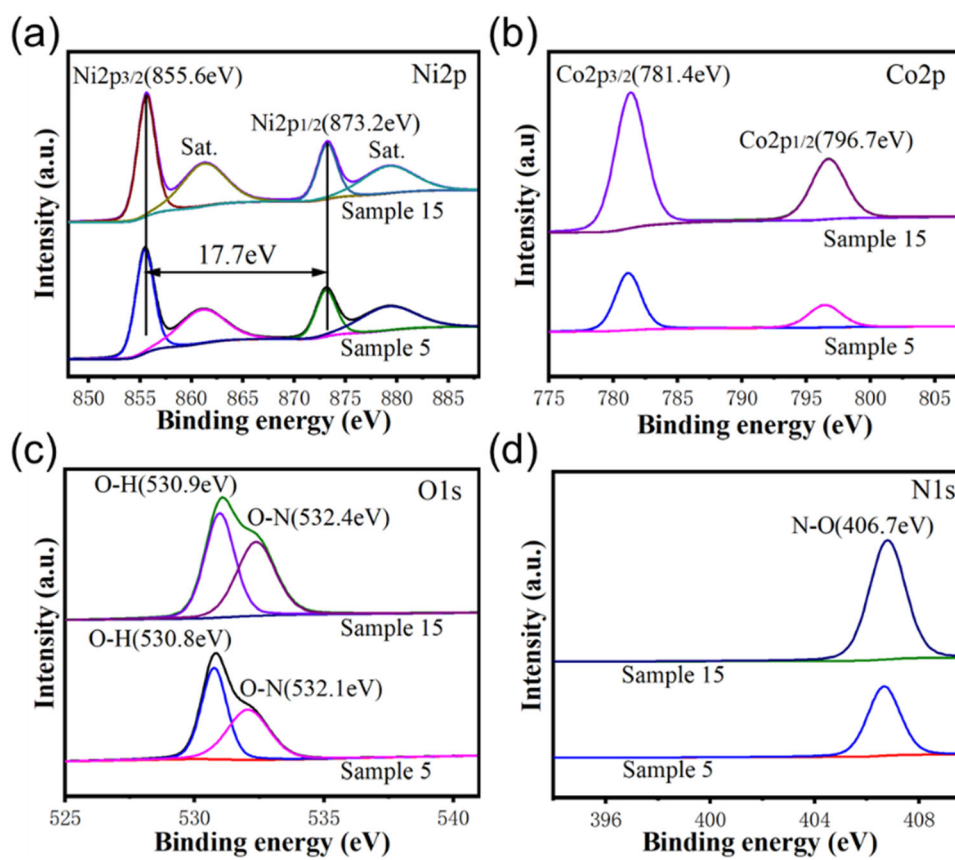
resistance of the electrochemical reaction. A larger diameter of the semicircular arc indicates a larger charge transfer resistance. The slope of the diagonal line in the low-frequency region represents the Warburg impedance, corresponding to the diffusion process of electrolyte ions in the electrode material. A large slope indicates a low Warburg impedance [40]. The intersection of the semicircular arc and the horizontal coordinate is the equivalent series resistance of the electrode, and the value represents the internal resistance of the electrode material [41]. From Fig. 5d, it can be seen that the equivalent series resistance of the samples decreased significantly after Co-doping, indicating that the conductivity of $Ni_3(NO_3)_2(OH)_4$ was improved. Meanwhile, Sample 15 has a larger slope representing a low Warburg impedance, indicating a faster ion diffusion rate and an excellent rate capability.

Apart from capacitances and rate capability, Co-doping improves also the cycle stability of the optimized sample. Cycled at a current density of 10 A/g,

Sample 15 remains 85.7% of its initial specific capacitance after 5000 cycles, while the capacity retention of Sample 0 is only 71.9%. Figure 5f further shows the morphology of the cycled Sample 15. After cycling, the sample still demonstrates a nanosized lamellar structure, highlighting its structural stability against electrochemical cycling.

Even though Co-doping is beneficial, the electrochemical performances of the electrode materials do not always increase with the increase of cobalt. Incorporation of Co into the lattice of $Ni_3(NO_3)_2(OH)_4$ nanosheets may provide additional active reaction sites, but there is an optimized Co-doping dosage to boost the Co–Ni bimetallic synergy. When the cobalt doping dosage excesses the optimal point, the specific capacitance is remarkably suppressed (Table S2), probably due to the limited electrolyte accessibility because of the decreased specific surface area and pore volume. Table S1 compares the electrochemical performance of typical $Ni_3(NO_3)_2(OH)_4$-based electrode materials. It is clearly

Fig. 4 Adsorption/desorption isotherms and pore size distribution curves (insets) of Sample 5 **a**, Sample 10 **b**, Sample 15 **c** and Sample 20 **d**
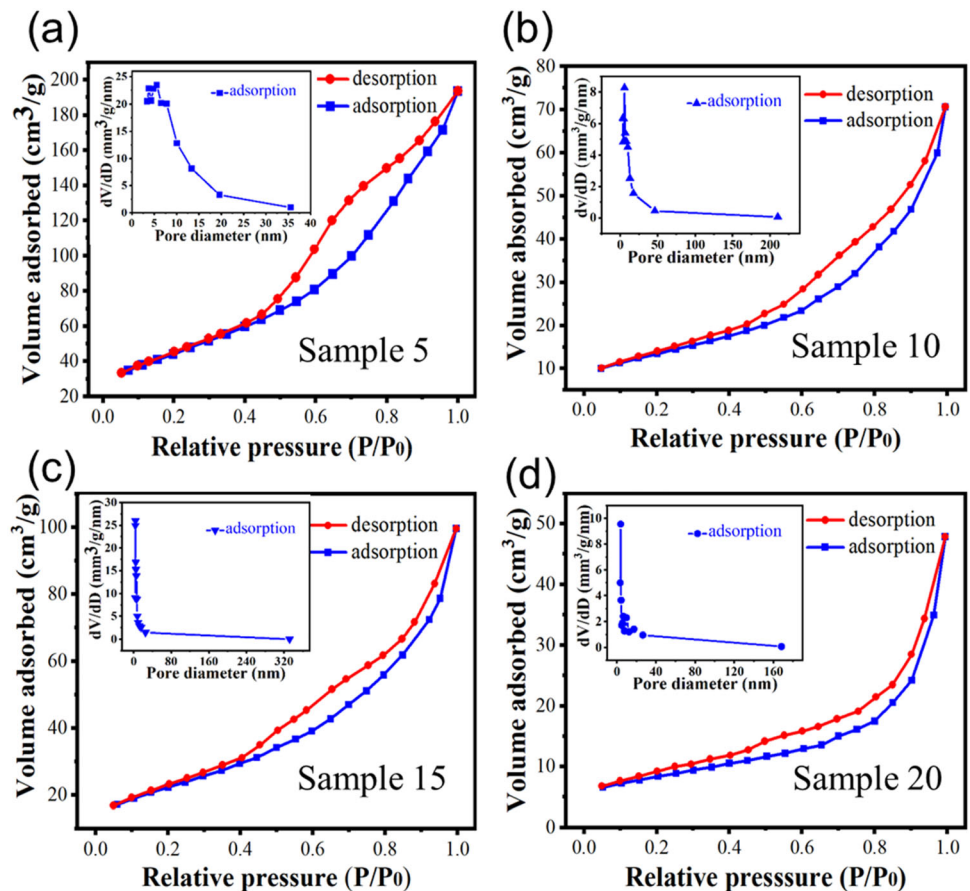

Table 1 BET-determined pore structures of samples with different Co-doping dosages

	Sample 0	Sample 5	Sample 10	Sample 15	Sample 20
Specific surface area (m^2/g)	113	162.7	47.9	80.4	28.9
Pore volume (cm^3/g)	0.317	0.3	0.1	0.2	0.07

shown that the performance of our Co-doped $Ni_3(NO_3)_2(OH)_4$ is comparable to the best reported data.

Achievement of excellent electrochemical performance at high mass loading is vitally important that the practical application of electrode materials. For this reason, the electrochemical performance of Sample 15 at different mass loading (3.45–15.05 mg/cm^2) was tested. As shown in Fig. 6a, the peak current value of the strength and area of redox peaks decrease with the increase of loading, due to the resistance increase of the thick electrode. When the mass loading increased to 15.05 mg/cm^2, the CV curve still delivers a pair of obvious redox peaks, indicating that the utilization rate of Sample 15 remains still high. The specific capacity and surface capacitance of Sample 15 can be

calculated from the GCD curve in Fig. 6b. At a current density of 1 A/g, the specific capacitance and surface capacitance of Sample 15 are 1062 F/g and 16 F/cm^2 for a load of 15.05 mg/cm^2, respectively (Fig. 6c). These data further demonstrate the beneficial influence of Co-doping on the electrochemical performance of the $Ni_3(NO_3)_2(OH)_4$ materials.

3.3 Characterization of asymmetric capacitors

To demonstrate the practical application potential of this strategy, an asymmetric capacitor was assembled using Sample 15 as the positive electrode and commercial AC (256F/g at 1A/g) as the negative electrode.
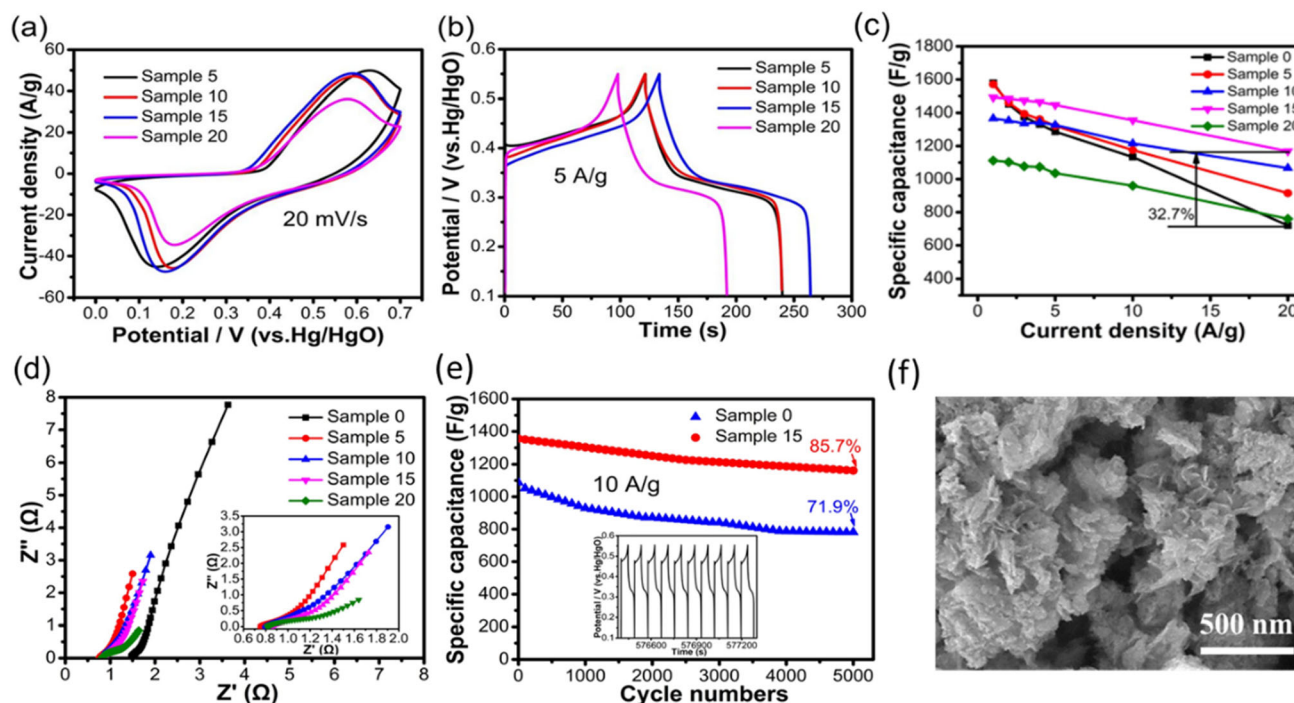
Fig. 5 **a** CV curves at the scan rate of 20 mV/s and **b** GCD curves at the current density of 5 A/g of Sample 5, Sample 10, Sample 15 and Sample 20. **c** Rate capability curves of different samples. **d** EIS curves of different samples (The inset is local enlarged image of EIS curves). **e** Cycling performance curves at the current density of 10 A/g of Sample 0 and Sample 15. **f** SEM of Sample 15 before and after cycling

The masses of the positive and negative electrodes had been matched according to Eq. 2. For this case, the loading mass of the positive (Sample 15) and the negative electrode is 5.1 and 11.9 mg, respectively. As shown in Fig. 7a, the CV curves at all scanning rates demonstrate similar rectangular shapes, indicating a high-rate capability. The highly reversible charge storage and release behavior of this capacitor can be illustrated from the symmetrical GCD curve in Fig. 7b. Figure 7c shows the energy density versus power density of the asymmetric capacitor determined by Eqs. 3 and 4 based on the total masses of both positive and negative electrodes. The capacitor achieves an energy density of 26 Wh/Kg at a power density of 2766 W/Kg, much higher than the performance of the $Ni_3(NO_3)_2(OH)_4$ porous

nanosheet//AC asymmetric capacitor ($\sim$ 14 Wh/Kg, 2766 W/Kg). In addition, Fig. 7d further shows the cycling stability of the asymmetric capacitor under a GCD test mode. After 3000 cycles, the specific capacity retention rate was 87.3% for the Co-doped asymmetric capacitor, also higher than that of $Ni_3(NO_3)_2(OH)_4$// AC device (82.6%) [8], demonstrating the multifaceted benefits of Co-doping.

4 Conclusion

In summary, $Ni_3(NO_3)_2(OH)_4$ electrode materials with different Co-doping amounts were prepared by a facile solution combustion method. Systematic analyses
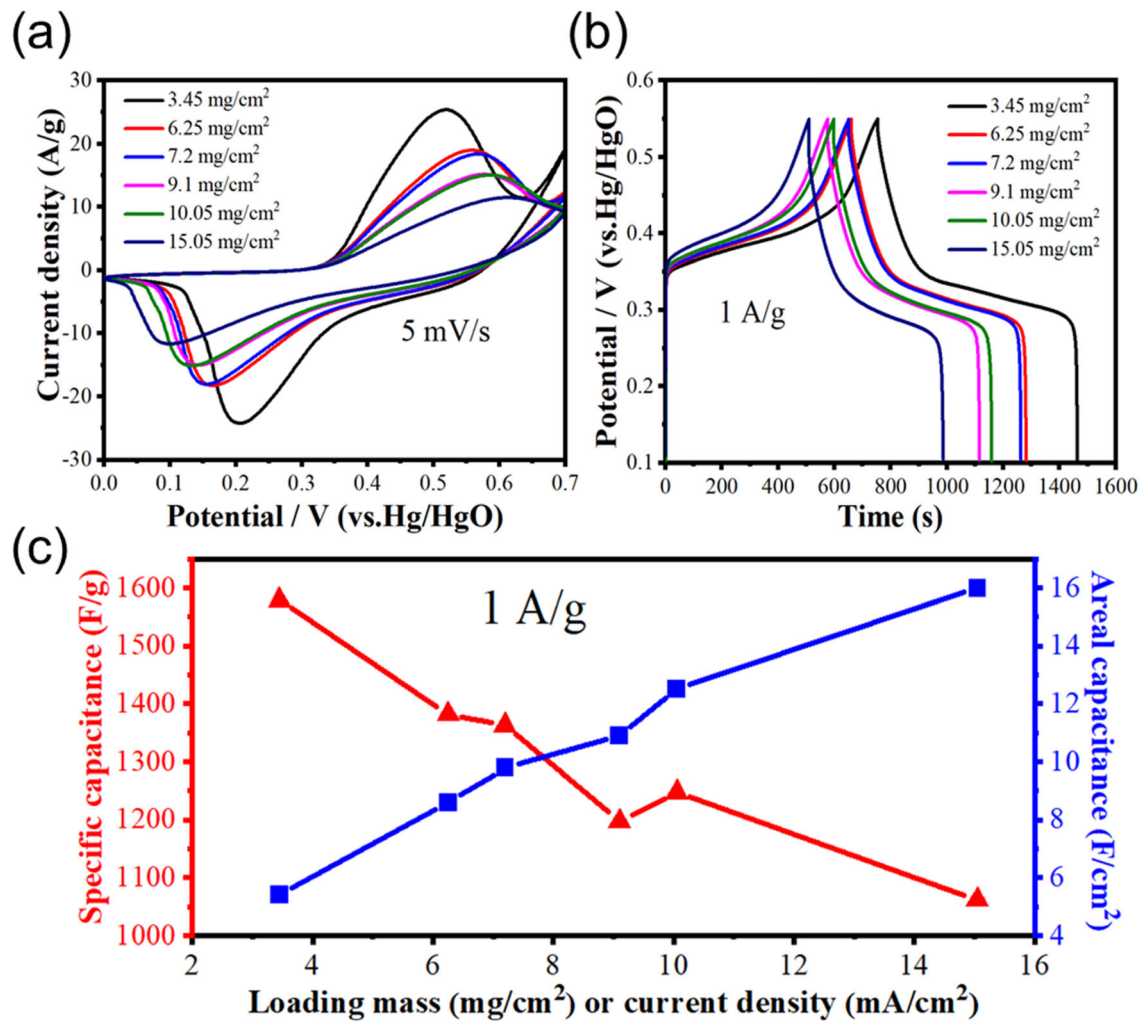
Fig. 6 a, **b** CV and GCD curves at different mass loadings of Sample 15. **c** Relationship between specific capacitance/ areal capacitance and mass loading/ current density

confirm that the cobalt element is doped into the lattice of $Ni_3(NO_3)_2(OH)_4$ as Co^{2+}. Electrochemical tests showed that Co-doping can significantly improve the rate capability and cycling stability of $Ni_3(NO_3)_2(OH)_4$. Among them, Sample 15 showed the best performance. The as-assembled asymmetric capacitors also showed both high energy and power density. The Co-doping and fast synthesis route in this work provide a novel idea to realize mass production of high-performance pseudocapacitive electrode materials.
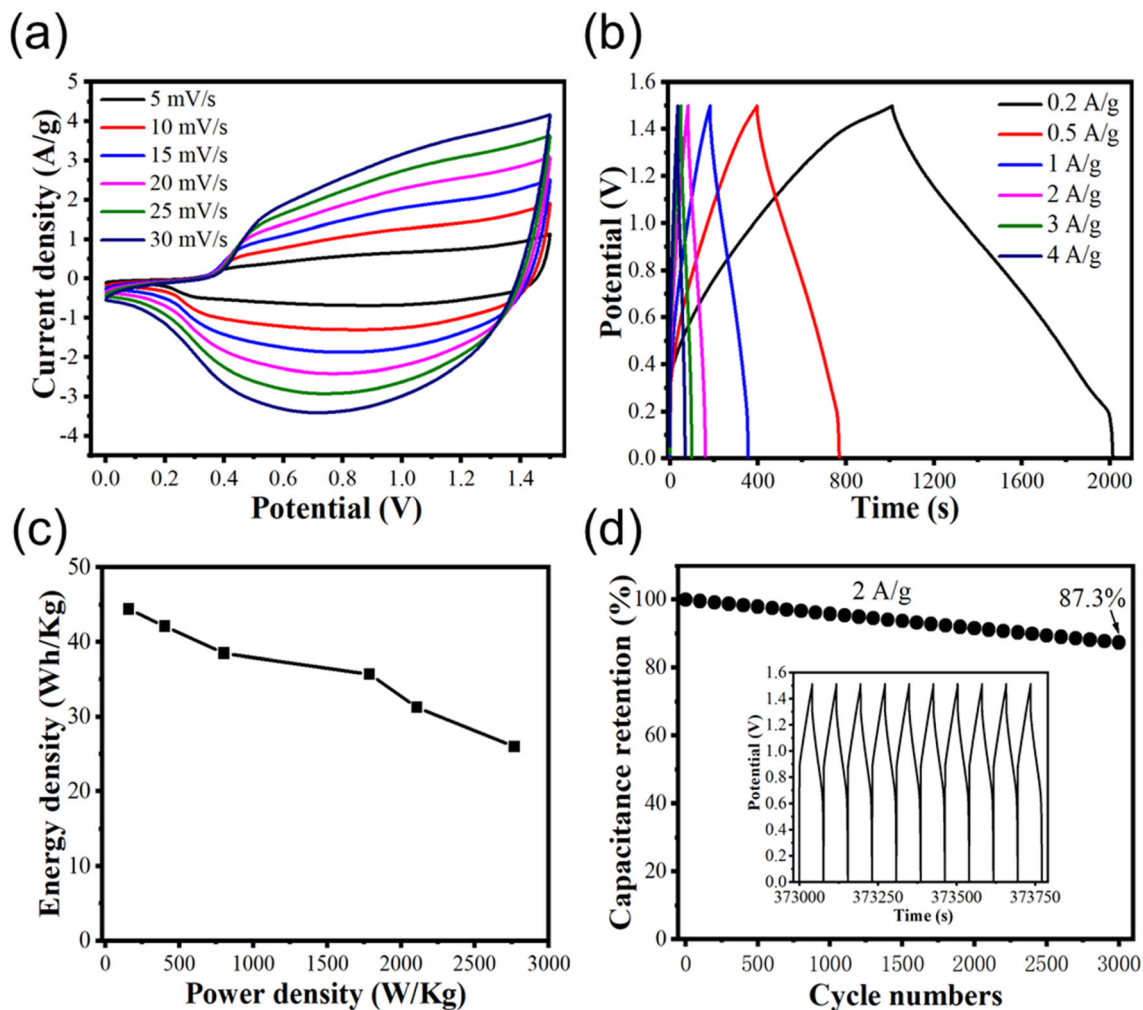
Fig. 7 CV curves **a**, GCD curves **b**, Ragone plot **c**, Cycling performance curve of the Sample 15//AC button capacitor **d**, the inset of panel shows the last 10 GCD curves

Author contributions

Each named author has substantially contributed to conducting the underlying research and drafting this manuscript.

Data availability

The data that support the findings of this study can be available from the corresponding author [LT Kang] upon reasonable request.

Declarations

Conflict of interest The named authors have no conflict of interest, financial or otherwise.

Supplementary Information: The online version contains supplementary material available at https://doi.org/10.1007/s10854-022-08604-z.

References

1. W. Hong, Y. Li, Y. Wu, G. Li, L. Jia, Mater. Chem. Front. **5**, 1438 (2021). https://doi.org/10.1039/d0qm00692k
2. R. Nasser, G.-F. Zhang, J.-M. Song, Electrochim. Acta (2020). https://doi.org/10.1016/j.electacta.2020.136198
3. G. Ni, F. Qin, Z. Guo, J. Wang, W. Shen, Electrochim. Acta (2020). https://doi.org/10.1016/j.electacta.2019.135270
4. Y. Yang, H. Niu, F. Qin et al., Electrochim. Acta (2020). https://doi.org/10.1016/j.electacta.2020.136667
5. Z. Yang, Y. Pei, X. Wang, L. Liu, X. Su, Comput. Theor. Chem. **980**, 44 (2012). https://doi.org/10.1016/j.comptc.2011.11.008
6. J. Wang, J. Li, Y. Liu, M. Wang, H. Cui, J. Mater. Sci. **56**, 3011 (2020). https://doi.org/10.1007/s10853-020-05446-0
7. Y. Zhao, N. Jiang, X. Zhang et al., Mater. Chem. Phys. **217**, 291 (2018). https://doi.org/10.1016/j.matchemphys.2018.06.082
8. M. Shi, M. Cui, L. Kang et al., Appl. Surf. Sci. **427**, 678 (2018). https://doi.org/10.1016/j.apsusc.2017.09.012
9. K. Tao, P. Li, L. Kang et al., J. Power Sources **293**, 23 (2015). https://doi.org/10.1016/j.jpowsour.2015.05.004
10. H. Liu, Y. Zhang, Q. Ke, K.H. Ho, Y. Hu, JJJoMCA Wang **1**, 12962 (2013)
11. B Jza, B Sya, B Cla, C My, SBJJoEC Yan (2020) 878
12. P Chang, F Yang, Y Cen, et al. (2021)
13. K.R. Sharma, N.S. Negi, J. Supercond. Novel Magn. **34**, 633 (2020). https://doi.org/10.1007/s10948-020-05753-2
14. Abhik, Banerjee, Sumit, et al. (2014) 6: 18844
15. B. Li, Y. Shi, K. Huang et al., Small **14**, e1703811 (2018). https://doi.org/10.1002/smll.201703811
16. M. Shen, S.J. Zhu, Z. Guo et al., Chem. Commun. **56**, 3257 (2020). https://doi.org/10.1039/d0cc00749h
17. G. Srikesh, A.S. Nesaraj, Mater. Technol. (2020). https://doi.org/10.1080/10667857.2020.1824147
18. S. Xu, T. Wang, Y. Ma, W. Jiang, ZJC Yang **10**, 4056 (2017)
19. Meng, Balamurugan, Jayaraman, Xuyang, N Hoon, J Hee (2017)
20. BC Kim, CJ Raj, WJ Cho, et al. (2014) 617: 491
21. DJJoPS Yang (2012) 198: 416
22. J. Xiao, L. Wan, S. Yang, F. Xiao, SJNL Wang **14**, 831 (2014)
23. D. Karuppiah, R. Palanisamy, A. Ponnaiah, S. Rengapillai, S. Marimuthu, Int. J. Energy Res. **44**, 7591 (2020). https://doi.org/10.1002/er.5492
24. Z. Yu, J. Hao, W. Li, H. Liu, Materials. (2019). https://doi.org/10.3390/ma12060843
25. G. Ali, G. Rahman, K.Y. Chung, Electrochim. Acta **238**, 49 (2017). https://doi.org/10.1016/j.electacta.2017.04.006
26. D. Zhang, X. Zhang, C. Yao, Y. Peng, C. Wang, YJJoPS Ma **196**, 5990 (2011)
27. H. Chen, J. Jiang, L. Zhang et al., J. Power Sources **254**, 249 (2014). https://doi.org/10.1016/j.jpowsour.2013.12.092
28. W Du, X Wang, J Zhan, X Sun, ZJEA Guo (2018) 296
29. H. Lai, Q. Wu, J. Zhao et al., Energy Environ. Sci. **9**, 2053 (2016). https://doi.org/10.1039/c6ee00603e
30. C. Tang, G. Li, L. Li, Chem. Lett. **37**, 1138 (2008). https://doi.org/10.1246/cl.2008.1138
31. M. Guo, J. Balamurugan, X. Li, N.H. Kim, J.H. Lee, Small **13**, 1701275 (2017). https://doi.org/10.1002/smll.201701275
32. D. Yang, J. Power Sources **198**, 416 (2012). https://doi.org/10.1016/j.jpowsour.2011.10.008
33. C Tang, G Li, LJCL Li (2008) 37: 1138
34. K.J.K. Beng Jit Tan, P.M.A. Sherwood, J. Am. Chem. Soc. **113**, 855 (1991)
35. J.P. Bonnelle, J. Grimblot, A. D'Huysser, J. Electron Spectrosc. Relat. Phenom. **7**, 151 (1975). https://doi.org/10.1016/0368-2048(75)80047-8
36. RBaGD A. M. Venezia, Surface and interface analysis **23**, 239 (1995)
37. WMR C. A. Tolman, W. J. Linn, C. M. King, R. C. Wendt, Inorgan. Chemi. **12**, 2770 (1973)
38. K.S.W. Sing, Pure Appl. Chem. **54**, 2201 (1982)
39. Q. Feng, F. Liu, J. Yuan, Q. Xu, Int. J. Electrochem. Sci. **15**, 2863 (2020). https://doi.org/10.20064/2020.04.26
40. L. Xie, L. Kang, Y. Li et al., NANO (2017). https://doi.org/10.1142/s1793292017500400
41. D. Hulicova, M. Kodama, HJCoM Hatori **18**, 2318 (2006)

Publisher's Note Springer Nature remains neutral with regard to jurisdictional claims in published maps and institutional affiliations.